Supplementary Materials

Axial electron-conduction engineering of single-atom copper catalyst for kinetic-fast oxygen reduction

Shuang Li[#] Shiyu Li[#] Jin Wang, Yanjie Wu, Jin Yan, Ke Liu, Yahui Yang*, Hui Su*

Key Laboratory of Chemical Biology and Traditional Chinese Medicine Research (Ministry of Education), Key Laboratory of Light Energy Conversion Materials of Hunan Province College, College of Chemistry and Chemical Engineering, Hunan Normal University, Changsha 410081, Hunan, China.
[#]Authors contributed equally.

Correspondence to: Prof. Yahui Yang, Prof. Hui Su, Key Laboratory of Chemical Biology and Traditional Chinese Medicine Research (Ministry of Education), Key Laboratory of Light Energy Conversion Materials of Hunan Province College, College of Chemistry and Chemical Engineering, Hunan Normal University, Changsha 410081, Hunan, China. E-mail: yangyahui2022@sina.com; suhui@hunnu.edu.cn

Experimental details

Morphology and structure characterization.

The powder X-ray diffraction (XRD) analysis was conducted using an Ultima IV instrument from Rigaku Corporation, Japan. Scanning electron microscope (SEM) imaging was performed on a Gemini 500 system from Japan. Transmission electron microscopy (TEM) was carried out using a JEM-2100F microscope from JEOL, Japan. Aberration-corrected high-angle annular dark-field transmission electron microscopy (AC-HAADF-TEM) was performed on a JEM-ARM200F from FEI, USA. X-ray photoelectron spectroscopy (XPS) was performed on an ESCALAB 250Xi system from

Thermo Fisher Scientific, USA. X-ray absorption fine structure (XAFS) measurements were performed at the BL14W1 beamline of the Shanghai Synchrotron Radiation Facility (SSRF), China. In-situ synchrotron radiation infrared spectroscopy (in situ SRIR) was conducted at the National Synchrotron Radiation Laboratory (NSRL), China. Electrochemical measurements were performed using a CHI 760E electrochemical workstation from Shanghai Chenhua, China and a RotatingRing-disk Electrode technique (DC DSR, PHYCHEMI).

Electrochemical characterization.

Catalyst ink was prepared by sonicating the mixture comprising the catalyst (5 mg), Nafion solution (5 wt.%, 30 μL), and solvent (1000μL, water/ethanol = 1:3, v/v) for several hours until a homogeneous suspension was formed.

Afterward, a certain amount of the catalyst ink (5 μL) was coated and dried on the surface of the polished glassy carbon electrode (3 mm) at room temperature, and the mass of catalyst deposited on the electrode is 3.57 gm^{-2}. All electrochemical measurements were performed on a CHI760E electrochemical workstation (CH Instruments, China) with a standard three-electrode system using a carbon rod, an Ag/AgCl (saturated KCl) electrode, and a glassy carbon electrode coated with catalyst serving as the counter, reference, and working electrodes, respectively. Polarization curves for the ORR were recorded at room temperature in O_2-saturated 0.1 M KOH aqueous solution at various rotation rates (400–1600 rpm). In this work, the final potential was calibrated into a reversible hydrogen electrode (RHE), unless otherwise noted.

The transfer electron number (n) of the ORR was calculated according to the Koutecky-Levich equation below:

$$\frac{1}{J} = \frac{1}{J_L} + \frac{1}{J_K} = \frac{1}{B\omega^{1/2}} + \frac{1}{J_K} \quad (1)$$

$$B = 0.62nFC_0\, D_0^{2/3} V^{-1/6} \quad (2)$$

where J is the measured current density and J_K and J_L are the charge-transfer kinetics

and the diffusion-limited current densities, respectively ω stands for the angular velocity of the rotating electrode(rad·s^{-1}), n is the electron-transfer number in ORR, F is the Faraday constant (96,485 C·mol^{-1}), and C0 is the bulk concentration of oxygen. D_0 indicates the diffusion coefficient of oxygen, and V is the kinematic viscosity of the electrolyte. C_0, D_0 and V in 0.1 M KOH electrolyte were 1.2 × 10^{-6} mol·cm^{-3}, 1.9 × 10^{-5} cm^2·s^{-1} and 0.01 cm^2·s^{-1}, respectively.

RRDE measurements were carried out to calculate the yield of hydrogen peroxide (H_2O_2%) and the corresponding electron transfer number (n) as follows:

$$H_2O_2(\%) = 200 \times \frac{I_r/N}{I_d + I_r/N} \tag{3}$$

$$n = 4 \times \frac{I_d}{I_d + I_r/N} \tag{4}$$

where I_d and I_r are the disk and ring currents, respectively. The Pt ring current collection efficiency N was determined to be 0.37.

Calculation for mass activity and turnover frequency.

The mass activity can be determined by considering the metal sites as the active sites. Initially, the metal content of the Ax-Cl-Cu/NC catalyst was calculated from the Cu loading mass on the electrode. Afterwards， the mass activity (A g_{metal}^{-1}) was calculated according to the following equation: the geometric electrode area (A) of 0.07 cm^{-2} and the metal loading mass of the electrocatalyst (M metal, g) were taken into account.

$$Mass\ activity = \frac{A \times J_k \times 10^{-3}}{\mathrm{M_{metal}}} \tag{5}$$

Similarly, by assuming each Cu atom in the catalyst as an active single-site, the number of active sites in the Ax-Cl-Cu/NC catalyst could then be calculated based on the Cu loading mass on the electrode. The turnover frequency (TOF) can be derived from the following equation:

$$TOF = \frac{J_K \times A \times N_e \times 10^{-3}}{4 \times M_{metal} \times N_A/M} \tag{6}$$

where J_k is the kinetic current density (mA cm^{-2}), Ne is the electron number per

Coulomb (6.24×10^{18}), M_{metal} is the metal loading mass on the electrode, N_A is Avogadro′s constant (6.02×10^{23}), and M is the molar mass of Cu (64 $gmol^{-1}$).

Assembly and electrochemical testing of Zn-air batteries (ZAB).

The liquid ZAB was evaluated using a cyclically home-made instrument under ambient atmospheric conditions. The electrolyte was composed of 6 M KOH with 0.2 M zinc acetate, and a flow of O_2 (20 sccm) was maintained into the electrolyte during the test to ensure O_2 saturation. The catalysts coated on the carbon paper were used as the membrane electrode assembly (MEA) of the cathode (catalysts coating area was controlled at 1 cm × 1 cm), and a zinc plate with an effective area of 1 cm × 1 cm served as the anode. The polarization curves were recorded by LSV at room temperature on a CHI 760E electrochemical work station. Both the current density and power density were normalized to the effective surface area of the air electrode. The specific capacity was calculated according to the following equations:

$$Specificcapacity = I \times t/w_{Zn} \quad (7)$$

where I is the applied current (A), t is the serving time (s), and w Zn stands for the weight of zinc consumed (g).

In XAFS measurements.

The in XAFS measurements were performed at the 1W1B station in the Beijing Synchrotron Radiation Facility (BSRF), China. The maximum current is 250mA of the storage ring of BSRF. The line station used a Si (111) double-crystal monochromator, and further detuning of 30% to remove higher harmonics when performing the Cu K-edge XAFS measurements. During In XAFS measurements, the Cu catalyst-coated carbon cloths was selected as working electrode in an alkaline solution by a homemade cell through a three-electrode system. Specifically, the 5 mg sample was evenly dispersed in 1mL solution (water/ethanol = 1:1, v/v) containing 20 μL Nafion. Then, the catalyst ink was deposited as the working electrode on the carbon paper (~1 cm× 1 cm), with the Capton film fixed on the back of the carbon paper to ensure that more opening sites can participate in ORR.

In situ SRIR measurements.

We conducted in situ SRIR measurements at the beamline BL01B of the National Synchrotron Radiation Laboratory (NSRL, China). In order to gain better infrared signals, electrochemical tests were performed in a homemade top-plate cell. Specifically, considering the vibration absorption of water molecules, we used a ZnSe crystal window and pressed the catalyst electrode close to the window to reduce the loss of infrared light. The SRIR tests were employed in reflection mode with a spectral resolution of 2 cm^{-1}. Systemic ORR measurements were made after the background spectrum of the catalyst electrode was measured at an open-circuit voltage, and the ORR potential ranged from 1.00 to 0.65 V.

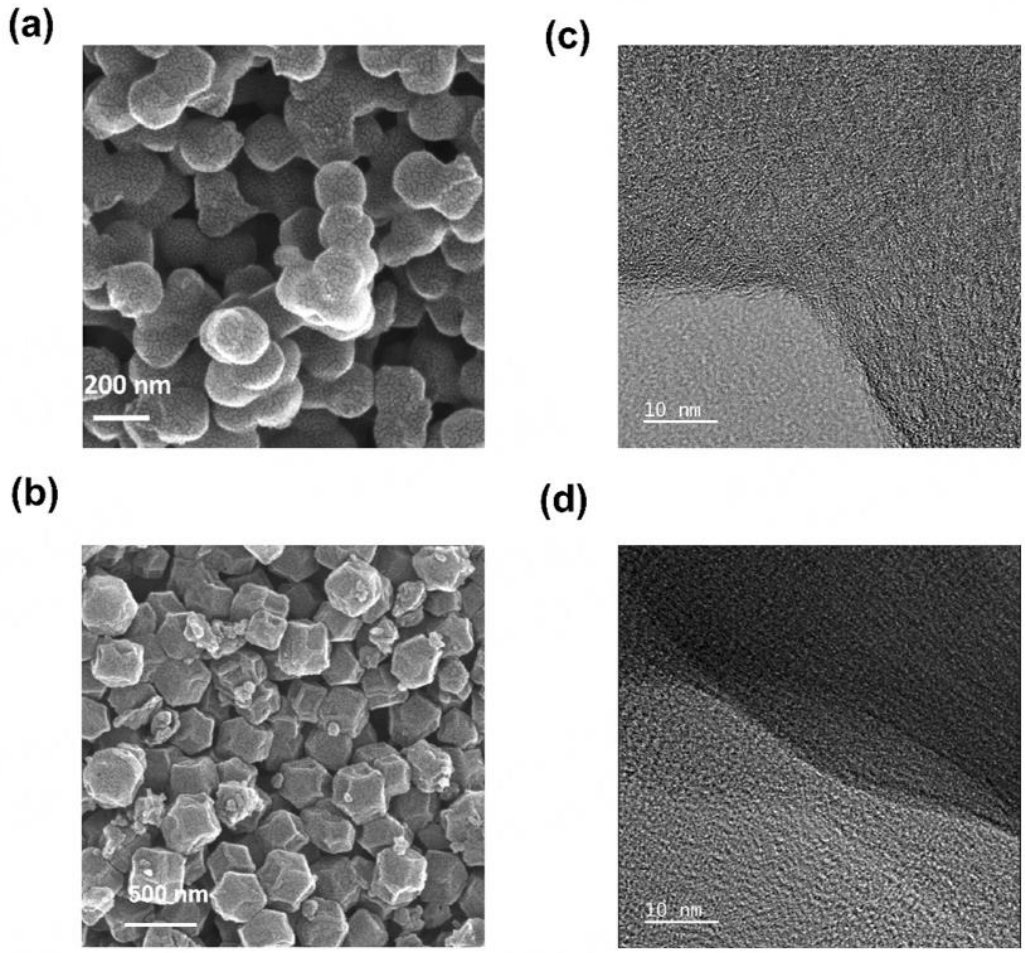

Fig. S1. (a,c) SEM image, (b,d) HRTEM image for Cu/NC and Ax-Cl-Cu/NC.

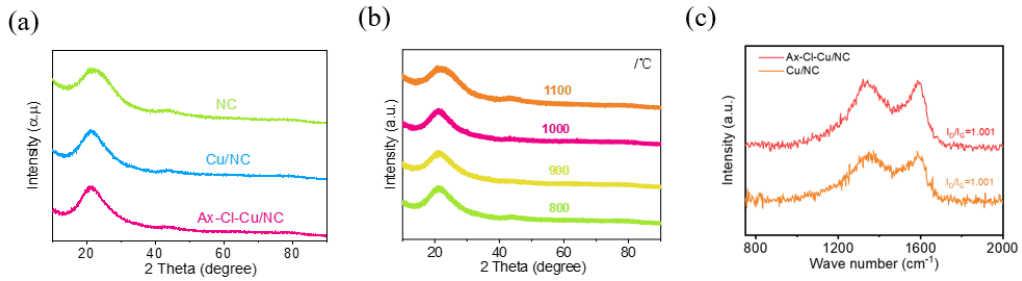

Fig. S2. (a) XRD patterns of Ax-Cl-Cu/NC, Cu/NC, and NC. (b) XRD patterns of Ax-Cl-Cu/NC at different temperatures. (c) Raman patterns of Ax-Cl-Cu/NC and Cu/NC.

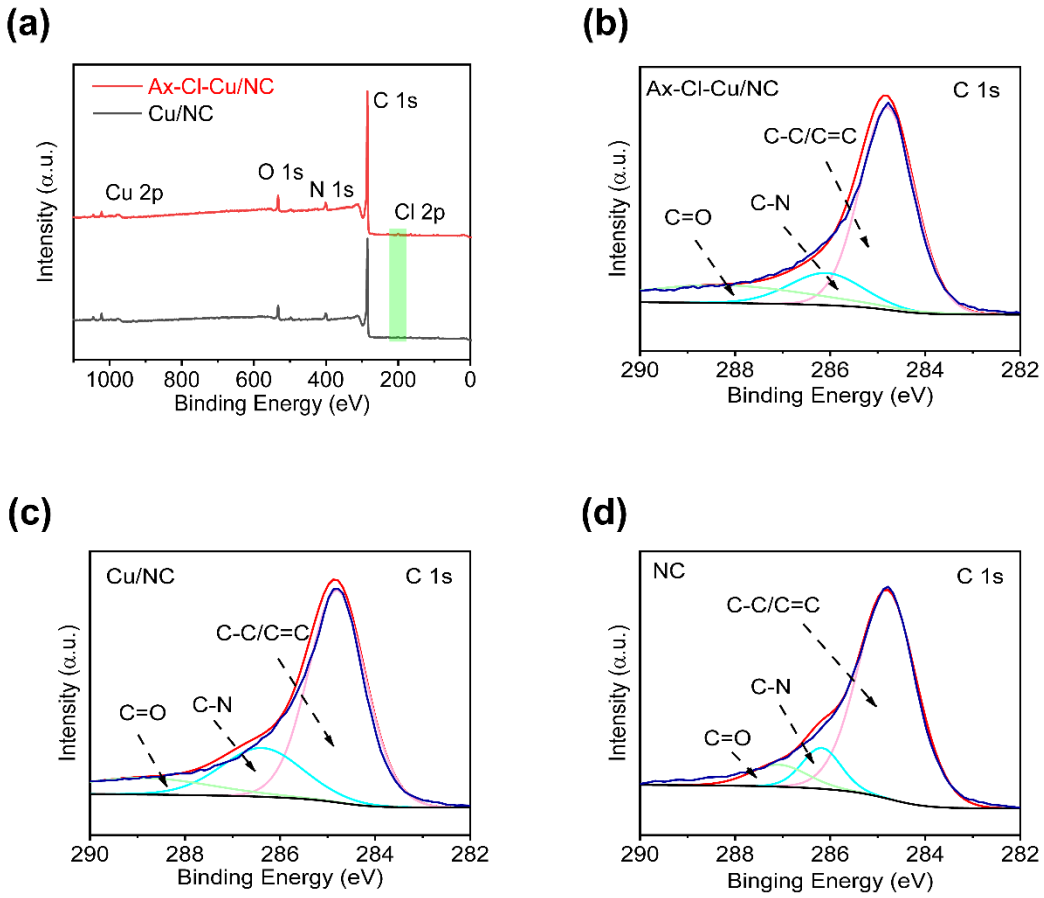

Fig. S3. (a) XPS survey spectra of Ax-Cl-Cu/NC, Cu/NC and (b) C 1s XPS spectra of Ax-Cl-Cu/NC, Cu/NC, NC.

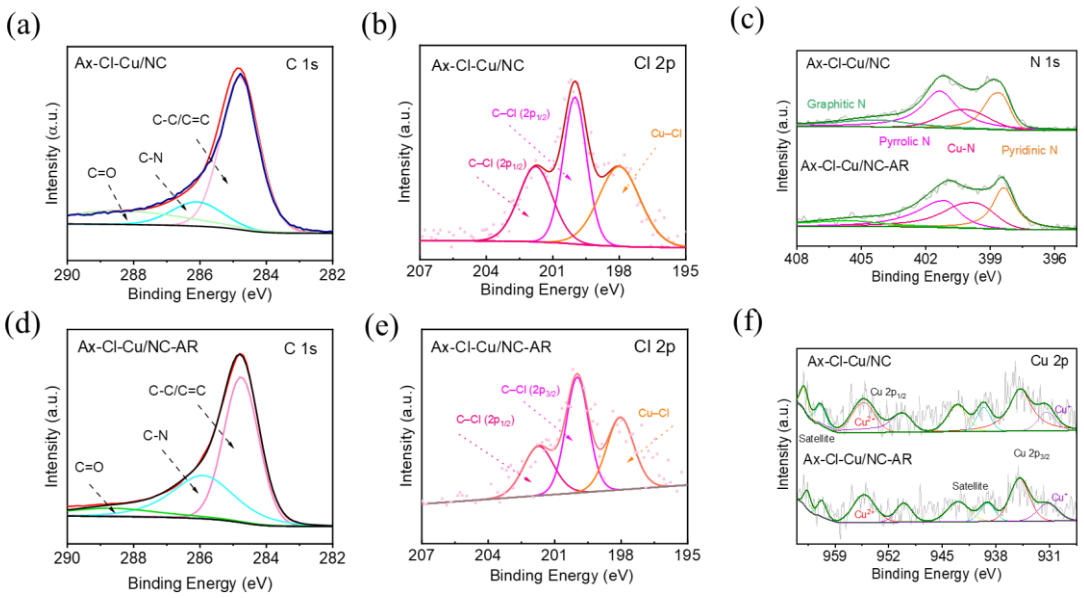

Fig. S4. XPS spectra of Ax-Cl-Cu/NC before (a) and after (b) the reaction.

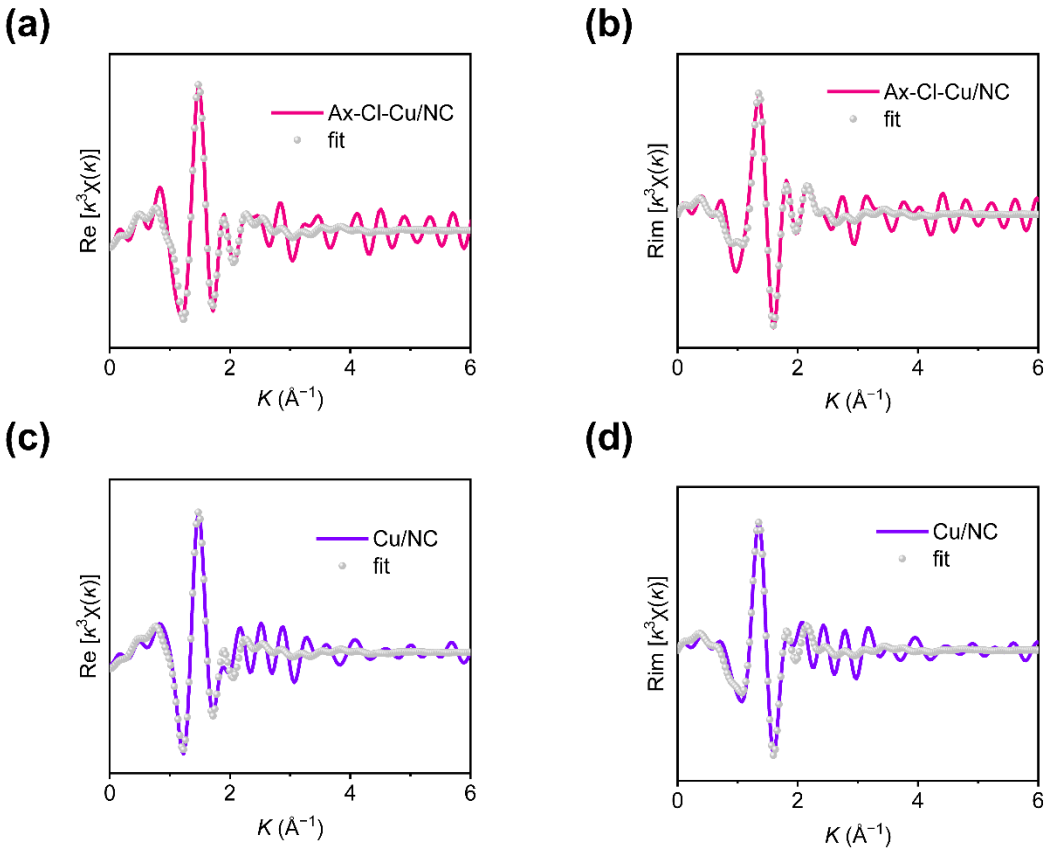

Fig. S5. (a,c) the Re (k^3 $\chi(k)$) oscillation curve for Ax-Cl-Cu/NC, Cu/NC, respectively. (b,d) the Rim (k 3 $\chi(k)$) oscillation curve for Ax-Cl-Cu/NC, Cu/NC, respectively.

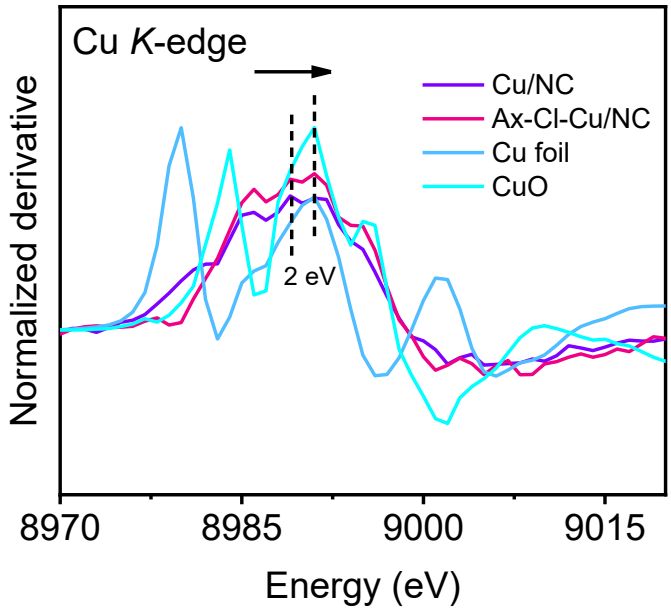

Fig. S6. Normalized derivative curves for Ax-Cl-Cu/NC and reference samples.

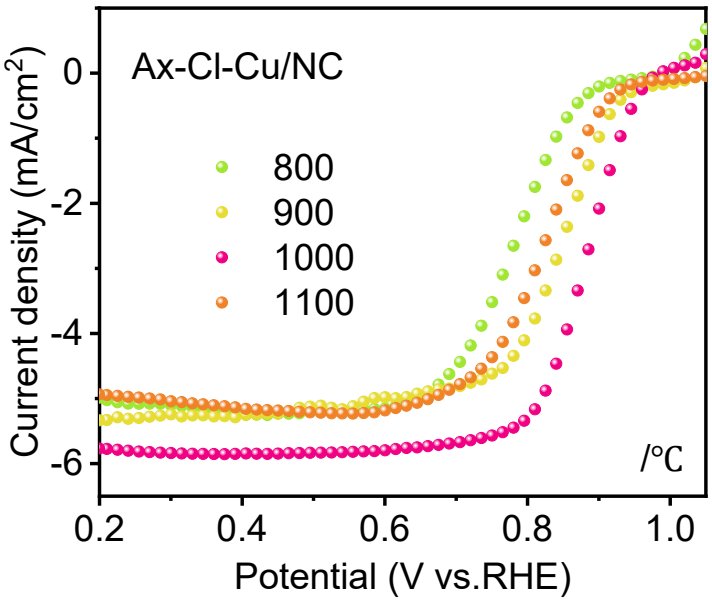

Fig. S7. Ax-Cl-Cu/NC LSV at 1600 rpm at different temperatures in O_2-saturated 0.1 M KOH.

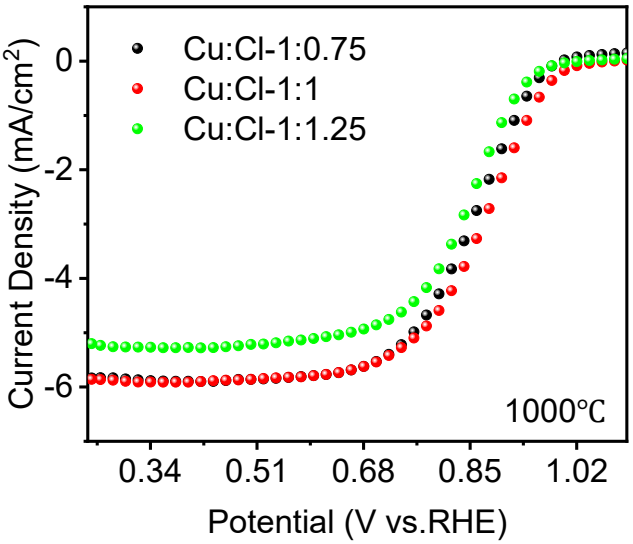

Fig. S8. LSV curves of ORR on catalysts with NaCl-to-Cu/NC mass ratios of 0.75:1, 1:1, and 1.25:1 in O_2-saturated 0.1 M KOH.

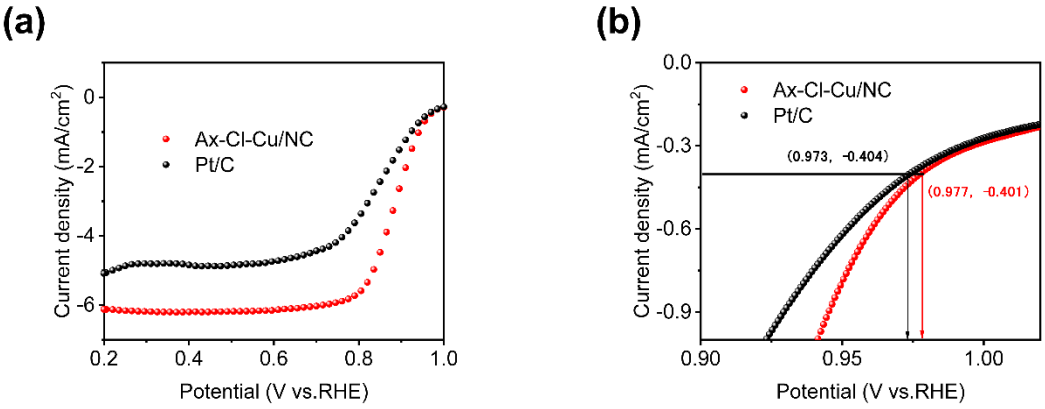

Fig. S9. (a) Polarization curves for Ax-Cl-Cu/NC and Pt/C under 0.1 M O_2-saturated KOH, 1600 rpm. (b) The onset potential can be determined based on the LSV curves when the ORR current is 5% of the diffusion-limited current.

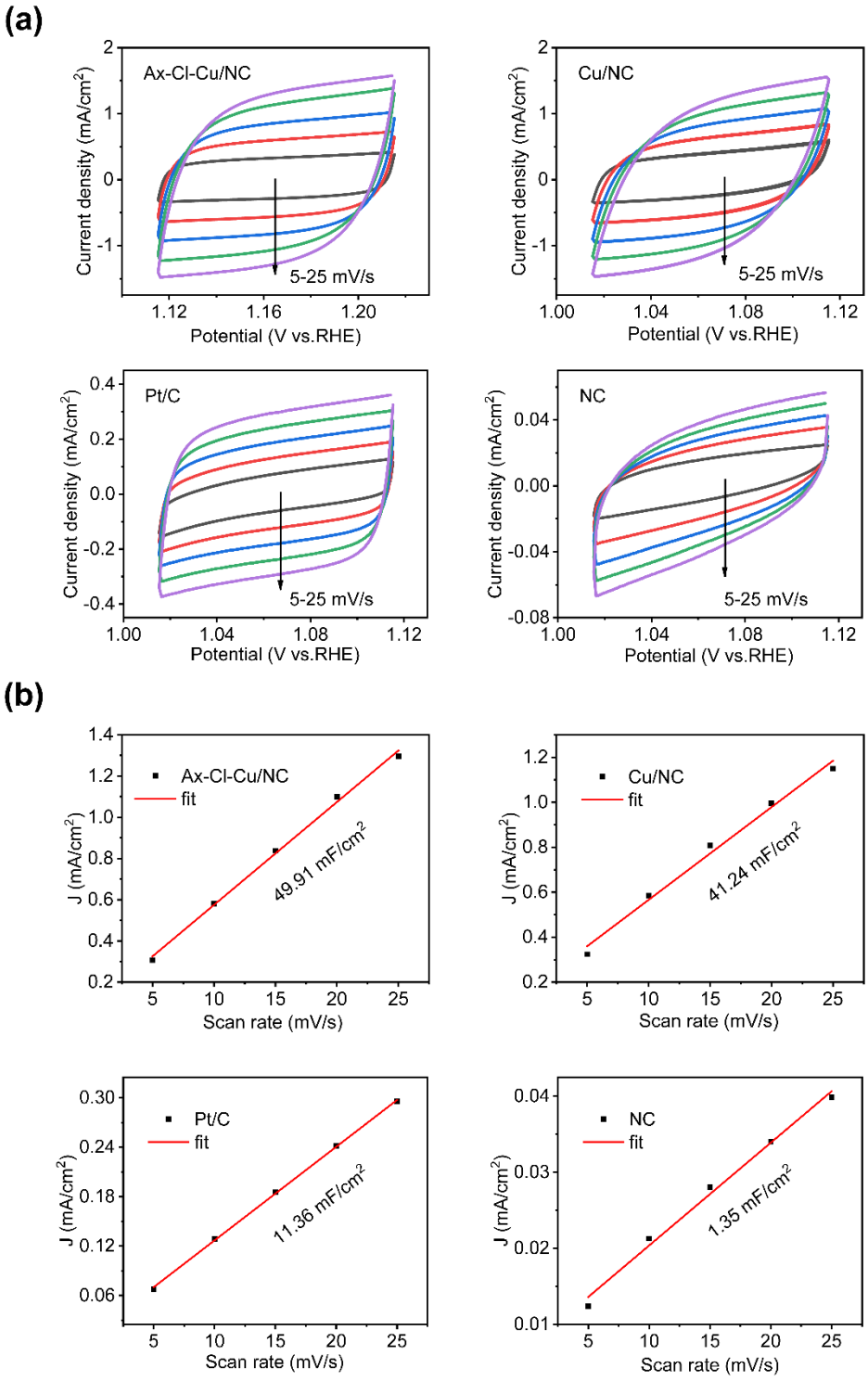

Fig. S10. (a) The cyclic voltammetry curves of Ax-Cl-Cu/NC、Cu/NC、Pt/C and NC catalyst at different scan rates (5–25 mV/s) and (b) corresponding electrochemical double-layer capacitance (Cdl).

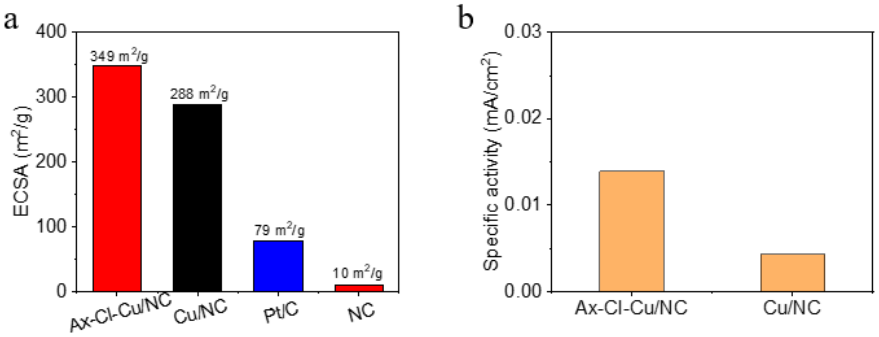

Fig. S11. ECSA based on double-layer capacitance Cdl and specific activity normalized to the ECSA.

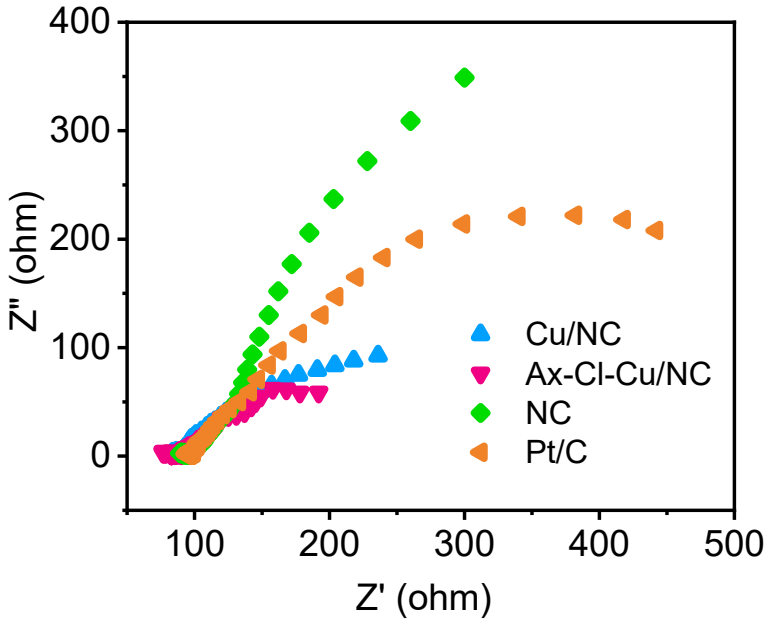

Fig. S12. Electrochemical Impedance Diagram (EIS) of catalysts for different samples.

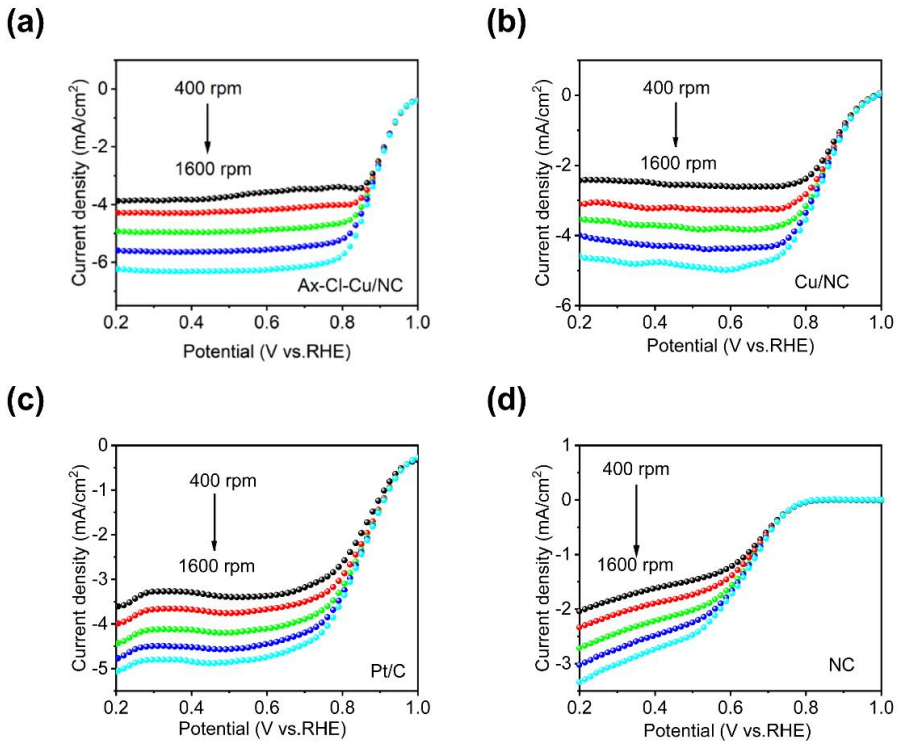

Fig. S13. LSV curves at various rotation rates of (a) Ax-Cl-Cu/NC, (b) Cu/NC, (c) Pt/C, and (d) NC.

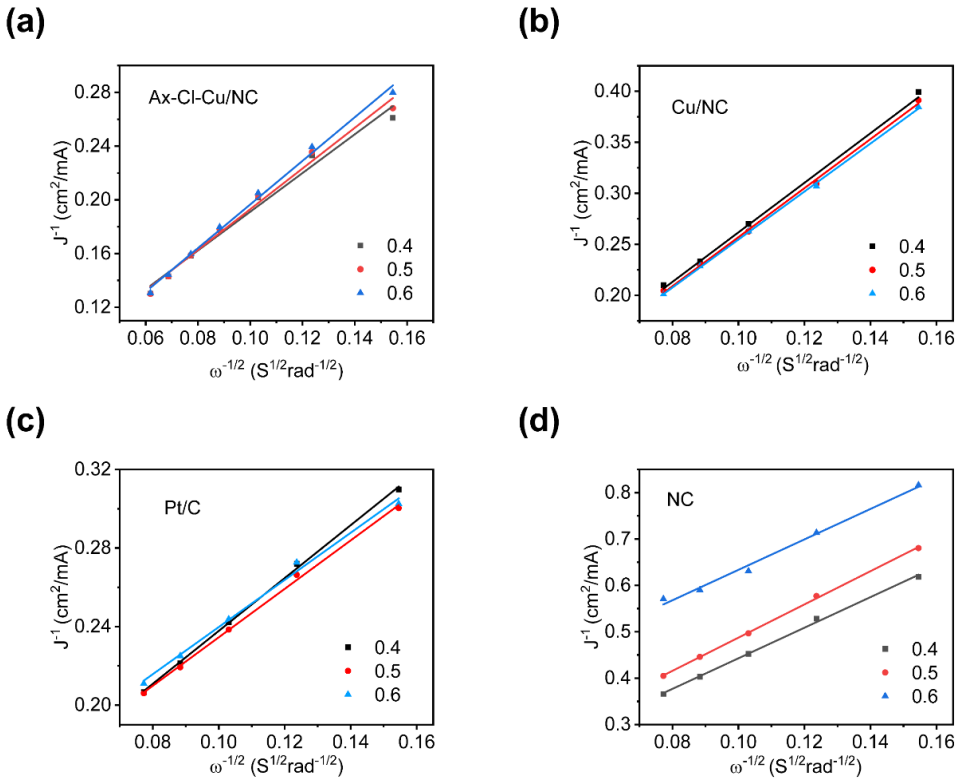

Fig. S14. Corresponding Koutecky-Levich plots of (a) Ax-Cl-Cu/NC, (b) Cu/NC, (c) Pt/C, and (d) NC.

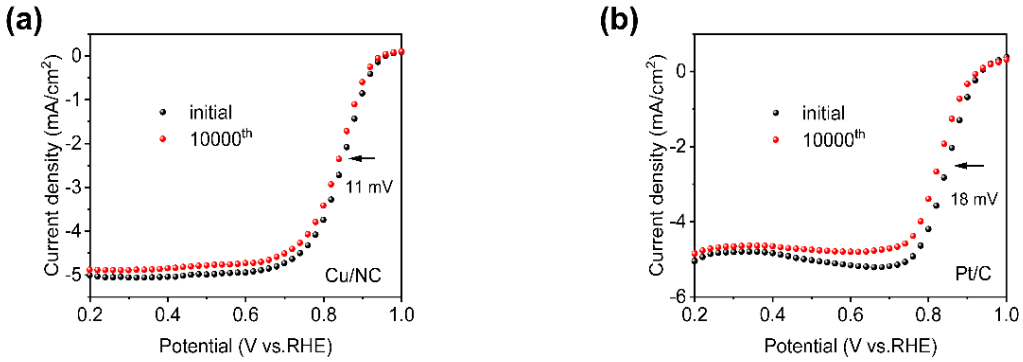

Fig. S15. Durability test plots (CA) of Cu/NC and Pt/C in 0.1 M KOH solution.

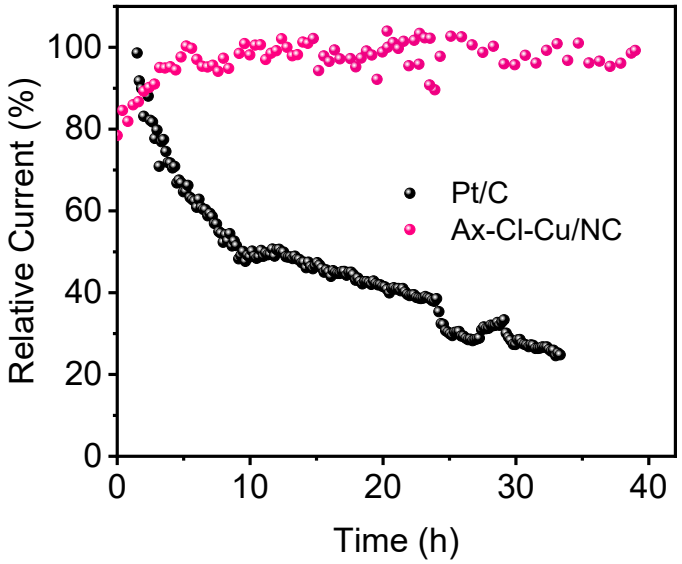

Fig. S16. Current-time chronoamperometric responses of Ax-Cl-Cu/NC and Pt/C.

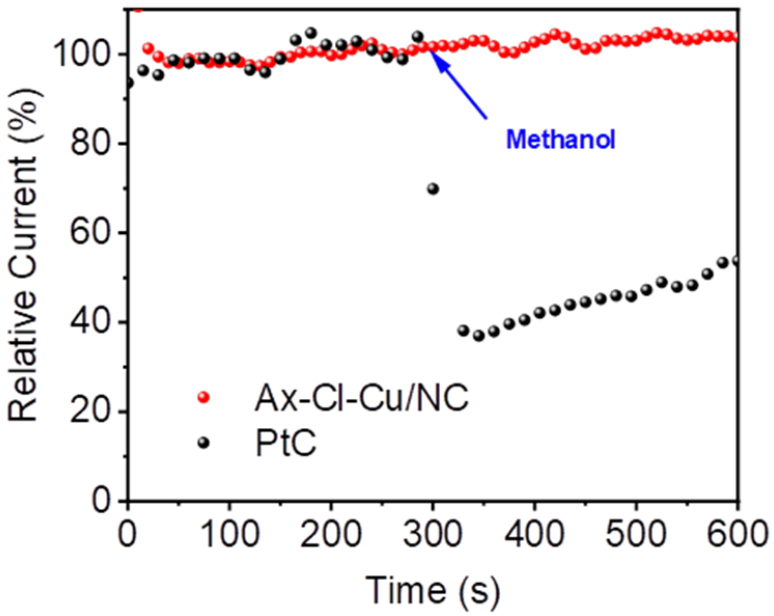

Fig. S17. Methanol tolerance test for Ax-Cl-Cu/NC and Pt/C.

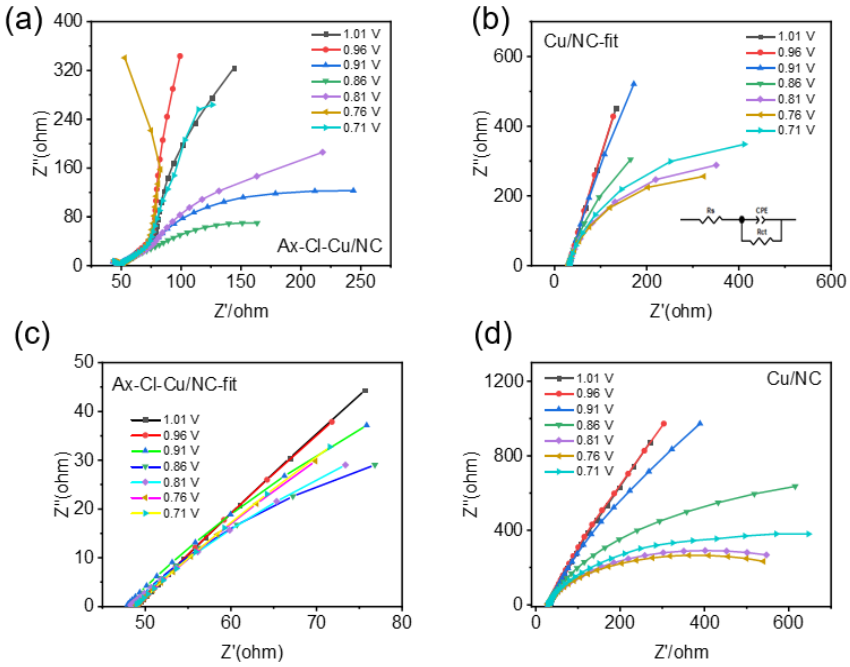

Fig. S18. Electrochemical Impedance Diagram (EIS) of (a,c) Ax-Cl- Cu/NC and (b,d) Cu/NC catalysts at different voltages.

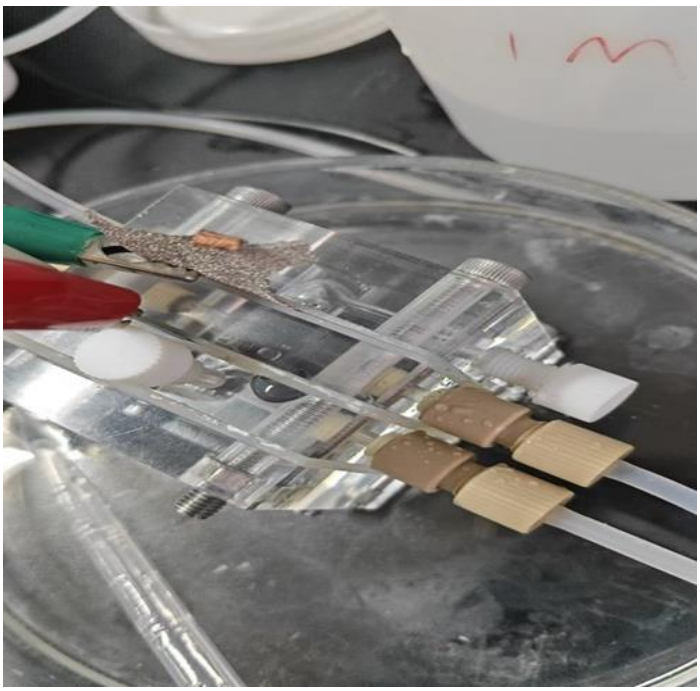

Fig. S19. Digital photograph of the Zn-air battery constructed using the Ax-Cl-Cu/NC catalyst as the cathode catalyst.

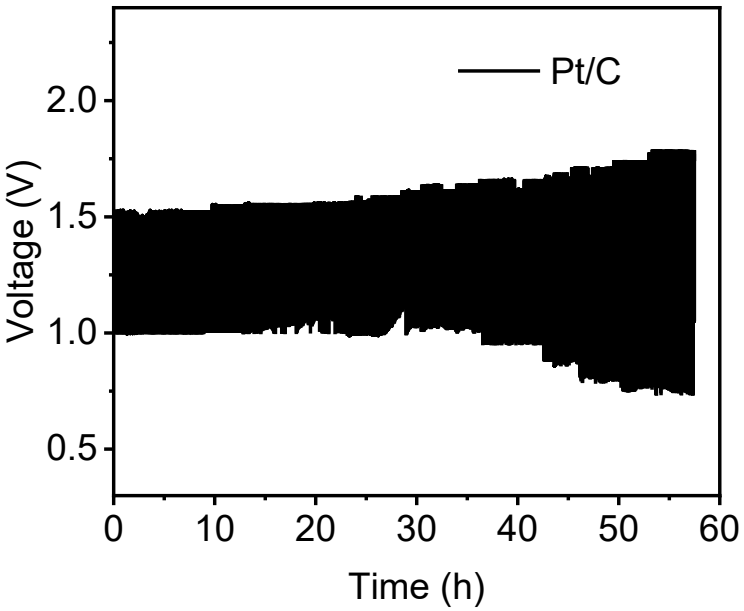

Fig. S20. Galvanostatic discharge-charge cycling curve performed under 10 mA cm^{-2} for the Pt/C based ZABs.

Table S1. The structural parameters extracted from quantitative EXAFS curve-fitting of samples using the ARTEMIS module of IFEFFIT.

Samples[a]	path	N[b]	R(Å)[c]	$\sigma(10^{-3}Å^2)$[d]	ΔE_0 (eV)	R-factor
Ax-Cl-Cu/NC	Cu-N	3.9±0.2	1.96±0.01	9.0±0.5	2.0	0.013
	Cu-Cl	1.0±0.1	2.05±0.01			
Cu/NC	Cu-N	3.9±0.1	1.95±0.01	9.0±0.3	1.0	0.015

[a]$S_0^2$was fixed as 1.0. Data ranges: $3.0 < k \leq 8.0$ Å^{-1},$1.0 \leq R < 3.0$ Å.

[b]N is the coordination number.

[c]R is the distance between absorber and backscatter atoms.

[d]$\sigma^2$is the Debye-Waller factor. R-factor is residual factor.

Table S2. The comparison of ORR performances of Ax-Cl-Cu/NC with other recently reported catalysts.

Catalysts	$E_{1/2}$ (V vs RHE)	References
Ax-Cl-Cu/NC	0.890	This work
FePc-Cl-CNTs	0.910	Angew. Chem. Int. Ed. 2025, e202504923[1].
Cu/Zn-NC	0.830	Angew. Chem. Int. Ed. 2021, 60, 14005-14012 [2].
Sb SAC	0.860	Angew. Chem. Int. Ed. 2021, 60, 21237-21241 [3].
Cu-SA/SNC	0.893	Energy Environ. Sci. 2019, 12, 3508-3514 [4].
Mn-NC-SA-950	0.852	J. Energy Chem. 2023, 80, 542-552 [5].
CR-Co/ClNC	0.930	Nat. Commun. 2024, 15, 1675 [6].
Se@NC-1000	0.850	Angew. Chem. Int. Ed. 2022, 61, e202114441 [7].

Ce SAs/PSNC	0.900	Adv. Mater. 2023, 35, 2302485 [8].
FeNSC-ZM	0.870	Chem. Eng. J. 2022, 444 136433 [9].
Cu-SACs-7	0.897	Small. 2023, 19, 2301075 [10].
S-Cu-ISA/SNC	0.918	Nat. Commun.2020, 11, 2041-1723 [11].

Table S3. Peak Assignments of In Situ SRIR Spectra and Corresponding References

Wavenumber (cm^{-1})	assignments	references
~1180	*OOH bending vibration	Angew. Chem. Int. Ed. 2026, 65, e21397 [12].
		ACS Catal. 2026, 16, 3, 2800–2813 [13].
		Appl. Catal. B 2025; 373: 125362 [14].
~900	*O stretching vibration	ACS Catal. 2026, 16, 3, 2800–2813[13] .
		Chem. Sci. 2026, Advance Article [15].
~1630	H-O-H bending vibration (interfacial water)	Appl. Catal. B 2025; 377: 125510 [16].
		J. Am. Chem. Soc. 2025, 147, 45, 41472–41480 [17].

Table S4. The comparison of Power density in ZABs of Ax-Cl-Cu/NC with other recently reported catalysts.

Catalyst	Power density ($mW\ cm^{-2}$)	References
Ax-Cl-Cu/NC	156.6	This work
BTC-Co-O-Cu-BTAa	200	J. Am. Chem. Soc. 2021, 143, 4064 [18].
(Ni,Cu)–NG	150.6	Nanoscale, 2021, 13, 10862 [19].

$CuMo_2ON$@NG	176.3	Nano Energy, 2021, 85, 105987 [20].
Cu_3P/MoP@C	156	Appl. Catal., B 2021, 297, 120415 [21].
Cu-SACs-7	165	Small. 2023, 2301075 [10].
CR-Co/ClNC	176.6	Nat. Commun. 2024, 15, 1675 [6].
Co_9S_8 @NSC	150.9	J. Alloys Compd. 2023, 948, 169792 [22].

REFEREFCE

1. M.N. Liu, Y.X. Liu, X. Zhang*, et al.* Altering the Symmetry of Fe-N-C by Axial Cl-Mediation for High-Performance Zinc-Air Batteries. Angew. Chem., Int. Ed., 2025; 64: e202504923. 10.1002/anie.202504923
2. M.M. Tong, F.F. Sun, Y. Xie*, et al.* Operando Cooperated Catalytic Mechanism of Atomically Dispersed Cu-N_4 and Zn-N_4 for Promoting Oxygen Reduction Reaction. Angew. Chem., Int. Ed. , 2021; 60: 14005-14012. 10.1002/anie.202102053
3. Y. Gu, B.J.J. Xi, H. Zhang*, et al.* Activation of Main-Group Antimony Atomic Sites for Oxygen Reduction Catalysis. Angew. Chem. Int. Ed., 2022; 61: e202202200. 10.1002/anie.202202200
4. Z.L. Jiang, W.M. Sun, H.S. Shang*, et al.* Atomic interface effect of a single atom copper catalyst for enhanced oxygen reduction reactions. Energy Environ. Sci, 2019; 12: 3508-3514. 10.1039/c9ee02974e
5. Y. Qin, C.Z. Guo, Z.H. Ou*, et al.* Regulating single-atom Mn sites by precisely axial pyridinic-nitrogen coordination to stabilize the oxygen reduction. J. Energy Chem., 2023; 80: 542-552. 10.1016/j.jechem.2023.01.048
6. M. Liu, J. Zhang, H. Su*, et al.* In situ modulating coordination fields of single-atom cobalt catalyst for enhanced oxygen reduction reaction. Nat. Commun.,

2024; 15: 1675. 10.1038/s41467-024-45990-w

7. H. Hu, J.J. Wang, B.F. Cui, *et al.* Atomically Dispersed Selenium Sites on Nitrogen-Doped Carbon for Efficient Electrocatalytic Oxygen Reduction. Angew. Chem. Int. Ed., 2022; 61: 10.1002/anie.202114441

8. L.L. Yin, S. Zhang, M.Z. Sun, *et al.* Heteroatom-Driven Coordination Fields Altering Single Cerium Atom Sites for Efficient Oxygen Reduction Reaction. Adv. Mater., 2023; 35: 2302485. 10.1002/adma.202302485

9. Y.Q. Dong, Z. Fang, D.L. Ou, *et al.* Rational fabrication of S-modified Fe-N-C nanosheet electrocatalysts for efficient and stable pH-universal oxygen reduction. Chem. Eng. J., 2022; 444: 136433. 10.1016/j.cej.2022.136433

10. X.Y. Yao, Y.Q. Zhu, T.Y. Xia, *et al.* Tuning Carbon Defect in Copper Single-Atom Catalysts for Efficient Oxygen Reduction. Small, 2023; 19: 2301075. 10.1002/smll.202301075

11. H.S. Shang, X.Y. Zhou, J.C. Dong, *et al.* Engineering unsymmetrically coordinated Cu-S_1N_3 single atom sites with enhanced oxygen reduction activity. Nat. Commun., 2020; 11: 3049. 10.1038/s41467-020-16848-8

12. C. Liu, K. Cheng, Q. Chen, *et al.* Synergy of Nickel Single-Atom and Heteroatoms Co-Doping in Carbon for Efficient Hydrogen Peroxide Electrosynthesis. Angew. Chem., Int. Ed., 2026; 65: e21397. 10.1002/anie.202521397

13. M.J. Wang, R. Ji, C. Huang, *et al.* Synergistic Strong-Weak Adsorption Coupling in the FeN_6–CoN_4 Dual-Site Modulates Oxygen Reduction Pathways via Oxygen Adsorbate Evolution-to-Dissociation Transition. ACS Catalysis, 2026; 16: 2800-2813. 10.1021/acscatal.5c08495

14. J. Liu, Z. Zhang, C. Han, *et al.* Ligand-modified nickel nitride for natural seawater H_2O_2 synthesis. Appl. Catal. B, 2025; 373: 125362. 10.1016/j.apcatb.2025.125362

15. S. Xu, Y. Zhang, Y. Peng, *et al.* Breaking the scaling relationship for oxygen reduction via amino-molecule-interface-mediated metallene electrocatalysts. Chemical Science, 2026; 10.1039/D5SC07852K

16. Z. Liu, M. Mo, B. Xiao*, et al.* Asymmetric coordination modulation on Co single-atom sites tunes selectivity of acidic oxygen reduction. Appl. Catal. B, 2025; 377: 125510. 10.1016/j.apcatb.2025.125510

17. H. Xia, M. Sun, D. Yang*, et al.* Phosphorus/Sulfur-Modulated p-Band Center of Pentagonal Carbon for Efficient Oxygen Reduction Reaction. J. Am. Chem. Soc. , 2025; 147: 41472-41480. 10.1021/jacs.5c11300

18. M.F. Sanad, A.R. Puente Santiago, S.A. Tolba*, et al.* Co–Cu Bimetallic Metal Organic Framework Catalyst Outperforms the Pt/C Benchmark for Oxygen Reduction. J. Am. Chem. Soc., 2021; 143: 4064-4073. 10.1021/jacs.1c01096

19. Y.T. Cheng, H.F. Wu, J.H. Han*, et al.* Atomic Ni and Cu co-anchored 3D nanoporous graphene as an efficient oxygen reduction electrocatalyst for zinc-air batteries. Nanoscale, 2021; 13: 10862-10870. 10.1039/d1nr01612a

20. J. Balamurugan, T.T. Nguyen, N.H. Kim*, et al.* Novel core-shell CuMo-oxynitride@N-doped graphene nanohybrid as multifunctional catalysts for rechargeable zinc-air batteries and water splitting. Nano Energy, 2021; 85: 105987. 10.1016/j.nanoen.2021.105987

21. M. Guo, M.J. Xu, Y. Qu*, et al.* Electronic/mass transport increased hollow porous Cu_3P/MoP nanospheres with strong electronic interaction for promoting oxygen reduction in Zn-air batteries. Appl. Catal., B, 2021; 297: 120415. 10.1016/j.apcatb.2021.120415

22. T. Yu, Y.T. Che, H. Fu*, et al.* N, S dual-doped carbon aerogels-supported Co9S8 nanoparticles as efficient oxygen reduction reaction electrocatalyst for zinc-air battery. J. Alloys Compd., 2023; 948: 169792. 10.1016/j.jallcom.2023.169792